Dynamics of Surface Deformation Induced by Dikes and Cone Sheets in a Cohesive Coulomb Brittle Crust

F. Guldstrand, S. Burchardt, Erwan Hallot, Olivier Galland

AGU PUBLICATIONS

JGR

Journal of Geophysical Research: Solid Earth

RESEARCH ARTICLE
10.1002/2017JB014346

Key Points:
- Laboratory models of surface deformation associated with dike and cone sheet emplacement in a cohesive Coulomb crust
- Dike emplacement systematically triggers surface uplift, in contrast to established elastic models
- We identify distinct surface deformation patterns and evolutions associated with dike and cone sheet emplacement

Supporting Information:
- Supporting Information S1

Correspondence to:
F. Guldstrand,
f.b.b.guldstrand@geo.uio.no

Citation:
Guldstrand, F., Burchardt, S., Hallot, E., & Galland, O. (2017). Dynamics of surface deformation induced by dikes and cone sheets in a cohesive Coulomb brittle crust. *Journal of Geophysical Research: Solid Earth*, *122*. https://doi.org/10.1002/2017JB014346

Received 18 APR 2017
Accepted 22 SEP 2017
Accepted article online 4 OCT 2017

Dynamics of Surface Deformation Induced by Dikes and Cone Sheets in a Cohesive Coulomb Brittle Crust

F. Guldstrand[1], S. Burchardt[2], E. Hallot[3], and O. Galland[1]

[1]Physics of Geological Processes, Department of Geosciences, University of Oslo, Oslo, Norway, [2]Centre for Mineralogy, Petrology and Geochemistry, Department of Earth Sciences, Uppsala University, Uppsala, Sweden, [3]Geosciences Rennes, UMR 6118, OSUR, CNRS-Université de Rennes 1, Rennes, France

Abstract The analysis of surface deformation associated with intruding magma has become an established method to study subsurface processes and intrusion architecture. Active subsurface magmatism induces deformation that is commonly modeled using static elastic models. To what extent, Coulomb failure of the crust affects surface deformation remains, so far, largely unexplored. In this contribution we present quantitative laboratory results of surface deformation induced by the emplacement of simulated dikes and cone sheets in a cohesive Coulomb material. The analysis of the experimental surface deformation shows that these intrusion types produce distinct and characteristic surface deformation signatures, which reflect the evolution of the intrusion at depth. Generally, dikes show a two-phase evolution while cone sheets develop gradually. In comparison, cone sheets induce larger uplifted areas and volumes than dikes relative to the depth of the injection source. Dike formation is, in turn, is likely accommodated, to a larger degree than cone sheets, by lateral opening of the host consistent with our current understanding of dike emplacement mechanics. Notably, only surface uplifts develop above the experimental dikes, consistent with a *viscous indenter* propagation mechanism, that is, a dike pushing ahead. The measured surface deformation patterns associated with dikes starkly contrast with established static, elastic models that predict local subsidence above the tip of a dike. This suggests that Coulomb failure of crustal rocks may considerably affect surface deformation induced by propagating igneous intrusions. This is especially relevant when a relatively high viscosity magma intrudes a weak host, such as unconsolidated sedimentary and volcaniclastic rocks.

1. Introduction

The analysis of surface deformation induced by ascending magma has developed into an established method to study the dynamics and geometry of subsurface magmatic activity (Amelung et al., 2000; Chadwick et al., 2011; Sigmundsson et al., 2015). This method postulates that the surface deformation reflects the combination of the shape of the intrusion, magma pressure distribution, subsurface propagation, and magma flow. Monitored surface deformation patterns are commonly fitted with geodetic models, in which the host rock deforms purely elastically (Dzurisin, 2006; Mogi, 1958; Okada, 1985).

However, the Earth's brittle crust is a cohesive, Coulomb material, implying that it does not only deform elastically. Recent field observations (Gudmundsson et al., 2008; Spacapan et al., 2017; Trippanera, Acocella, & Ruch, 2014) and modeling results (Abdelmalak et al., 2012; Haug et al., 2017; Pollard, 1973; Scheibert, Galland, & Hafver, 2017) show that brittle shear deformation may be significant in accommodating the emplacement of intrusions and the propagation of their tips. In addition, focal plane mechanisms constrained from dike-induced microseismicity dominantly involve shear failure of the host rock (Ágústsdóttir et al., 2016; White et al., 2011). These studies suggest that brittle shear deformation, which is generally not accounted for in geodetic models, may be nonnegligible during dike emplacement. Currently, it is not known to which extent intrusion-induced brittle deformation affects surface deformation patterns.

In this study, we explore the surface deformation patterns induced by sheet intrusions in a cohesive, Coulomb brittle host through quantitative laboratory models. The experimental procedure uses a cohesive fine-grained silica flour as model crust, and a molten, low-viscosity vegetable oil as model magma. This procedure builds on the setup and materials developed in Galland et al. (2006), the proof-of-concept of surface deformation shown in Galland (2012), and a parametric study of dykes versus cone sheet emplacement by

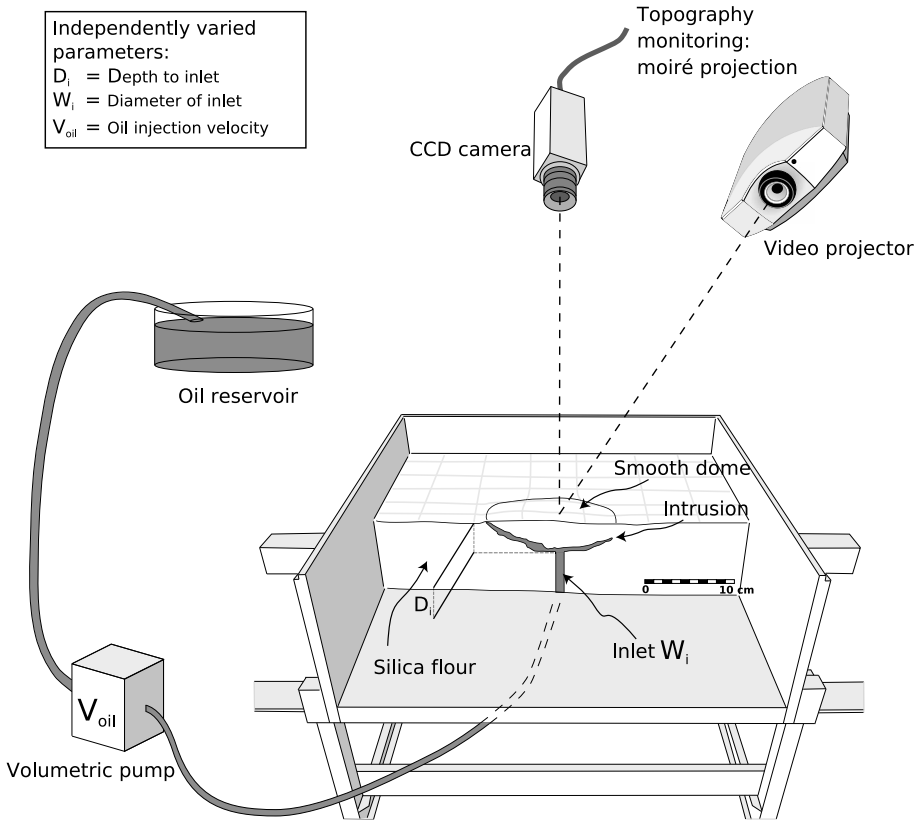

Figure 1. Schematic illustration of the experimental setup (modified from Galland, 2012; Galland et al., 2006). Oil is injected through a circular inlet using a volumetric pump into a 40 cm wide square box containing silica flour. The surface deformation induced by the resulting intrusion is periodically monitored using a moiré monitoring system. To control the shapes of the intrusions, the depth, D_i, and diameter, W_i, of the inlet, and the injection velocity of the oil, V_{oil}, were systematically varied (Galland et al., 2014).

Galland et al. (2014). This study presents a analysis of the large surface deformation data sets acquired during the experiments described in Galland et al. (2014).

During these experiments, the intrusion of the oil into the flour induced surface deformation that we monitored through a moiré projection method (Figure 1) (Bréque et al., 2004). We systematically analyzed the surface deformation associated with the two intrusions types, dikes, and cone sheets (Figure 2), from most of the experiments from Galland et al. (2014). Here we quantified how these two intrusion types induce distinguishable patterns of surface deformation.

2. Experimental Setup and Method

The experimental series used in this study are from those of the experiments of Galland et al. (2014) for which surface deformation data were available. In the experiments, (1) the inlet diameter (2, 5, and 10 mm), W_i; (2) the injection velocity (0.017 to 0.21 m s^{-1}), and (3) the injection depth (2 to 10 cm), D_i, were varied independently (Figure 1). The inlet was a cylindrical tube with circular section, the internal diameter of which affected the initial conditions of the models along with parameters (2) and (3) and so the geometry of the produced intrusions. Galland et al. (2014) showed that depending on the combination of the values of these three parameters, dikes, cone sheets, or "hybrid" intrusions that exhibit both dike and cone sheet characteristics are spontaneously produced (Figures 2 and 3). In the present study, we focus on the analysis of the surface deformation patterns associated with the development of the dikes and cone sheets.

We used the generic experimental protocol designed by Galland et al. (2006, 2009, 2014) and Galland (2012), in which the model materials are fine-grained silica flour and molten vegetable oil, to simulate brittle rocks and magma, respectively. The flour consists of fine (~15 μm), angular grains of crystalline silica flour under

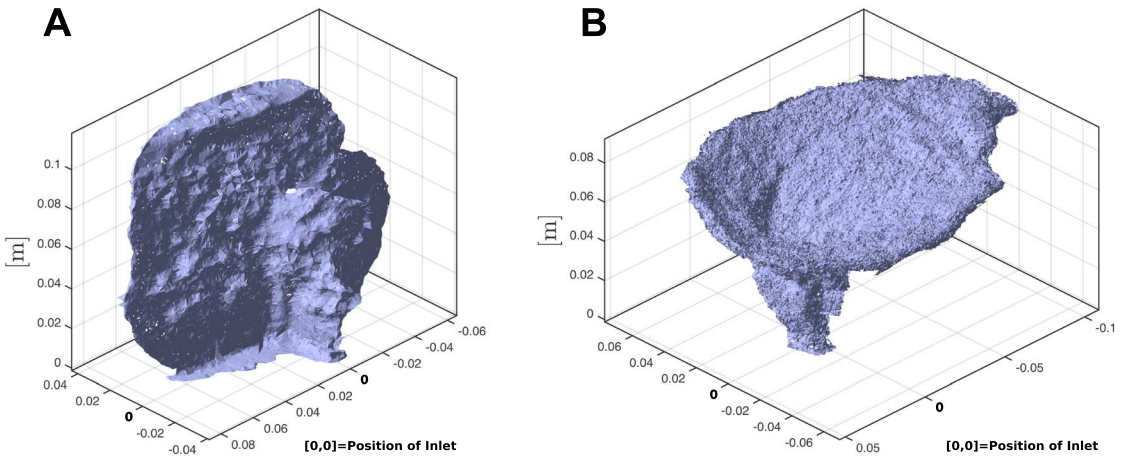

Figure 2. Meshed point clouds created through the use of Structure-from-Motion software MicMac (Galland et al., 2016) for two experimental intrusions produced using our laboratory setup, (a) dike and (b) cone sheet; 0 marks the position of the inlet.

the product name M400, manufactured in Belgium by Sibelco. It has a cohesive strength of 369 ± 44 Pa, a friction coefficient of 0.81 ± 0.06 (corresponding to an angle of internal friction of ~39°), and a tensile strength of 100 Pa (Galland, 2012; Galland et al., 2009).

The model magma consists of Végétaline, a vegetable oil produced in France by Unilever. Végétaline oil is solid at room temperature and melts at ~31°C (Galland et al., 2006). Molten, it is a Newtonian fluid with a weak temperature-dependent viscosity (Galland et al., 2006). Using these materials, a generic experiment consists in injecting oil into the flour to generate an intrusion. At the injection temperature of ~50°C, the oil has a viscosity of 0.02 Pa s and a density of 890 kg m^{-3}. Silica is chemically incompatible with the oil, such that oil percolation within the flour is limited during injection and oil intrusion is dominantly accommodated by

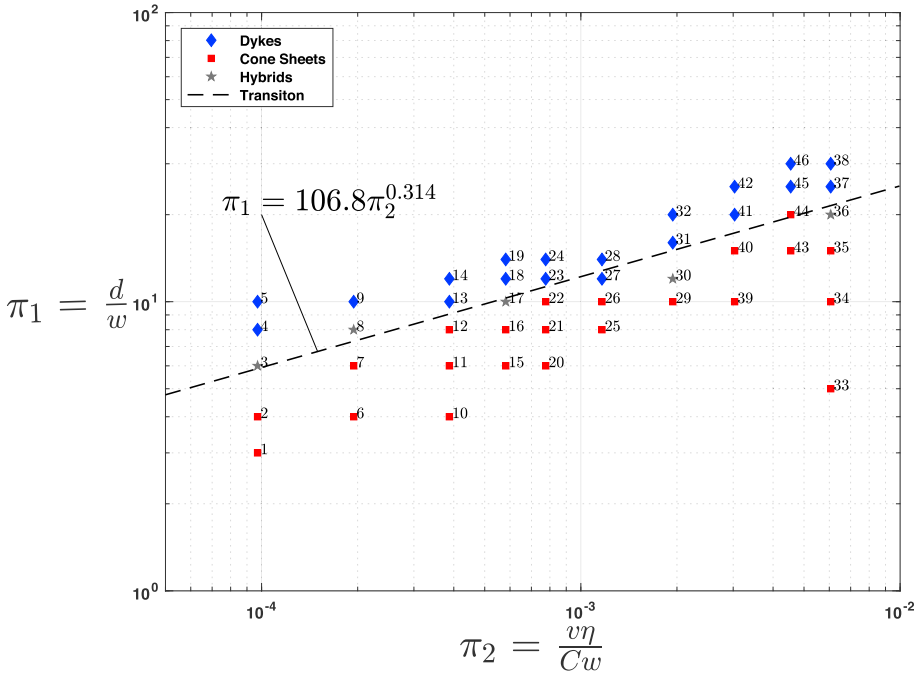

Figure 3. The experiments of Galland et al. (2014) for which surface deformation monitoring was applied. The dimensionless logarithmic plot distinguishes dikes (blue diamonds), cone sheets (red squares), and hybrid intrusions (grey stars). Π_1 is a geometric ratio of depth to width of the inlet. Π_2 is a dynamic ratio including the intruding oil velocity and viscosity divided by the cohesion of flour and width of inlet.

deformation of the flour (Galland et al., 2006). The effects of the cooling of the oil against the flour can be neglected due to the short intrusion durations (less than or up to about 1 min), being much shorter than the rate of cooling.

The suitability of the materials and the scaling of the models are discussed in detail by Galland et al. (2006), Galland et al. (2014), and Galland (2012, see also references therein). In brief, 1 cm in our models represents 100–1000 m in nature; the resulting stress ratio implies that the model crust should be 13×10^3 to 250×10^3 times weaker than its geological prototype (Abdelmalak et al., 2016). The model magma scales assuming that the ratios of viscous stresses in the magma to the cohesion of the host are identical in model and in nature (Galland et al., 2014). Magma velocities have been measured in nature to be on the order of $1–10^{-2}$ m s^{-1}. Our pumping apparatus allow for oil velocities of $10^{-3}–10^{-1}$ m s^{-1}. As magma viscosities cover a wide range ($10–10^7$ Pa s), the corresponding relevant model viscosities must range from 4×10^{-9} to 75 Pa s, which our model magma fulfills. In this scaling, the oil dominantly represents intermediate to felsic magma.

To prepare an experiment, a known mass of silica flour was first poured into a square, 40 cm wide, acrylic glass box with a bottom aluminum plate, to which an inlet was attached. It was then compacted using a high-frequency shaker (Houston Vibrator, model GT-25) to reach a controlled bulk density of 1050 kg m^{-3}. During compaction, a metal plate and a bubble level were placed onto the flour to ensure a flat and horizontal initial upper surface for each model, as well as homogeneous, repeatable experimental initial conditions. Before compaction, a plug was inserted into the inlet to prevent silica flour from clogging the inlet during compaction. The plug was then removed before injecting the oil.

During the experiments, a volumetric pump injected the oil at constant flow rate through the inlet, and a pressure sensor continuously recorded the oil pressure variations at a defined distance below the inlet. As the oil intruded, it triggered subtle surface deformation only in the central region of the box, up to ~15 cm from its lateral walls, enough to assume that boundary effects can be neglected during the experiments. The deformation was periodically monitored using a moiré projection system (Bréque et al., 2004; Galland, 2012). This method produces a time series of digital elevation models (DEMs) of the evolving model surface. It offers a spatial horizontal resolution of <1 mm and a raw elevation precision of ~0.2 mm. Subsequent smoothing of the DEMs improved the vertical accuracy to ~0.1 mm. The duration of a complete scan of the surface of a model was ~1 s, which is assumed to indicate the maximum error on the time at which each DEM was obtained. We have chosen to set the time of each DEM at the beginning of each scan. For the present work, the successive DEMs were captured at temporal steps of 1.5 s. As the durations of most of the experiments lasted up to approximately a minute, the resolution and accuracy of the method are adequate to record temporal evolutions but fail for the few very short experiments that lasted only a few seconds. We used the pressure measurements to limit cumulative errors on timescales. In the generic protocol, the moment at which the oil erupts at the model surface defines both the end of the experiment and of the DEM measurement. The accuracy on the durations of the experiments is <1 s. After an experiment, the oil solidifies for about 45 min, after which the resulting intrusion can be excavated to study its final shape (Figure 2). For some experiments minor oil flow downward along the circular inlet could be observed upon excavation.

3. Surface Deformation Results

Galland et al. (2014) performed 43 experiments for which surface deformation data were captured before, during, and after the oil injection, and among which 18 produced dikes and 19 produced cone sheets. The time series of DEMs show that surface deformation in all the experiments exhibits a common qualitative behavior. At an early stage of the injection, the surface lifts up, forming a gentle (elevation <1 mm), symmetrical dome with a quasi-central zone of maximum uplift (Figure 4a). Then, as injection proceeds, the dome develops a substantial asymmetry mostly marked by a point of maximum uplift that migrates toward the periphery of the uplifted zone (Figures 4b and 4c).

Nevertheless, significant differences can also be extracted from the DEMs, consistently with Galland (2012) , who qualitatively showed that surface deformation patterns evolve as a function of the underlying intrusion geometry. In the following, we systematically compare the surface deformation patterns induced by the formation of experimental dikes to those associated with the cone sheets. To do so, we analyzed, for each

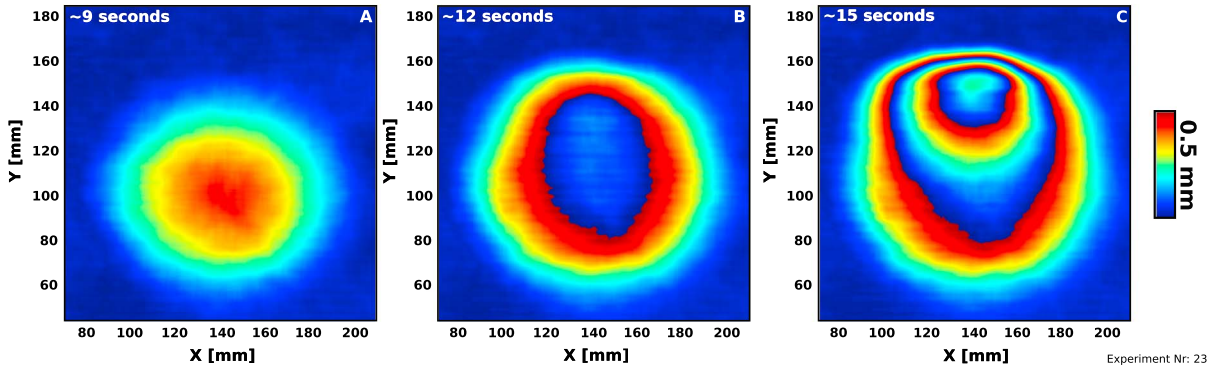

Figure 4. Maps of surface deformation captured for a representative dike experiment at an (a) initial, (b) intermediate, and (c) late stage during oil injection. The uplift has been wrapped in fringes where one fringe corresponds to 0.5 mm of uplift. Formation of a gentle symmetrical dome (Figure 4a) and an asymmetry that initiates amplifies with time (Figures 4b and 4c). The maps show a cropped area limited to the affected uplifted area. The dike was produced using an inlet width of 0.5 cm, a D_i = 6 cm, and an injection velocity of ~80 mL/min.

experiment, the temporal evolution of (1) the maximum uplift (h_m), (2) the uplifted area (A), and (3) the uplifted volume (V_{up}; Figure 5).

Figure 6 displays the evolution of h_m, A, and V_{up} for a representative cone sheet and dike experiment. During cone sheet experiments, h_m generally shows an almost steady, nearly linear increase through time. Conversely, during dike experiments, h_m generally exhibits a two-stage evolution, with an initial phase of moderate uplift, followed by a second stage of rapid uplift prior to eruption. The areal extent of the domed surface, A, exhibits a similar development through both the dike and cone sheet experiments: initially, A increases rapidly and then tends to asymptotically approach a stable value. Similarly, the uplifted volumes V_{up} for both the dike and cone sheet experiments increase linearly during the experiments. These results are consistent with those of Galland (2012).

A difficulty in analyzing raw data is that the experiments are not directly comparable (cf. Figure 6). For instance, the duration of the experiments varied from a few seconds to almost 1 min. Therefore, in order to make direct comparisons, we introduce a dimensionless time $\tau = t/t_e$, where t is the time at a given time step of an experiment and t_e is the duration, that is, the time to the eruption of the same experiment, such that τ may vary from 0 to 1, from the beginning to the end of an experiment. The values of maximum uplift

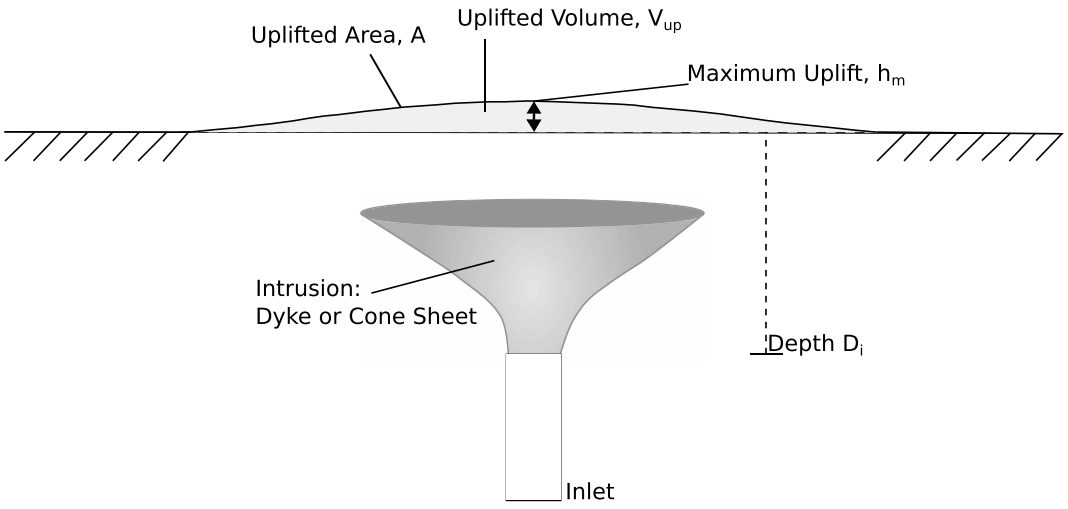

Figure 5. Illustration of the physical parameters used to quantify the surface deformation induced by an intrusion at each time step of an experiment (i.e., each 1.5 s from the beginning of the oil injection). The maximum uplift, h_m, corresponds to the maximum elevation. The uplifted area, A, is quantified as the 2-D projection defined by the largest continuous patch of points uplifted above a threshold value of 0.1 mm from the DEM of the initial horizontal surface. The uplifted volume, V_{up}, integrates the elevations over the uplifted area.

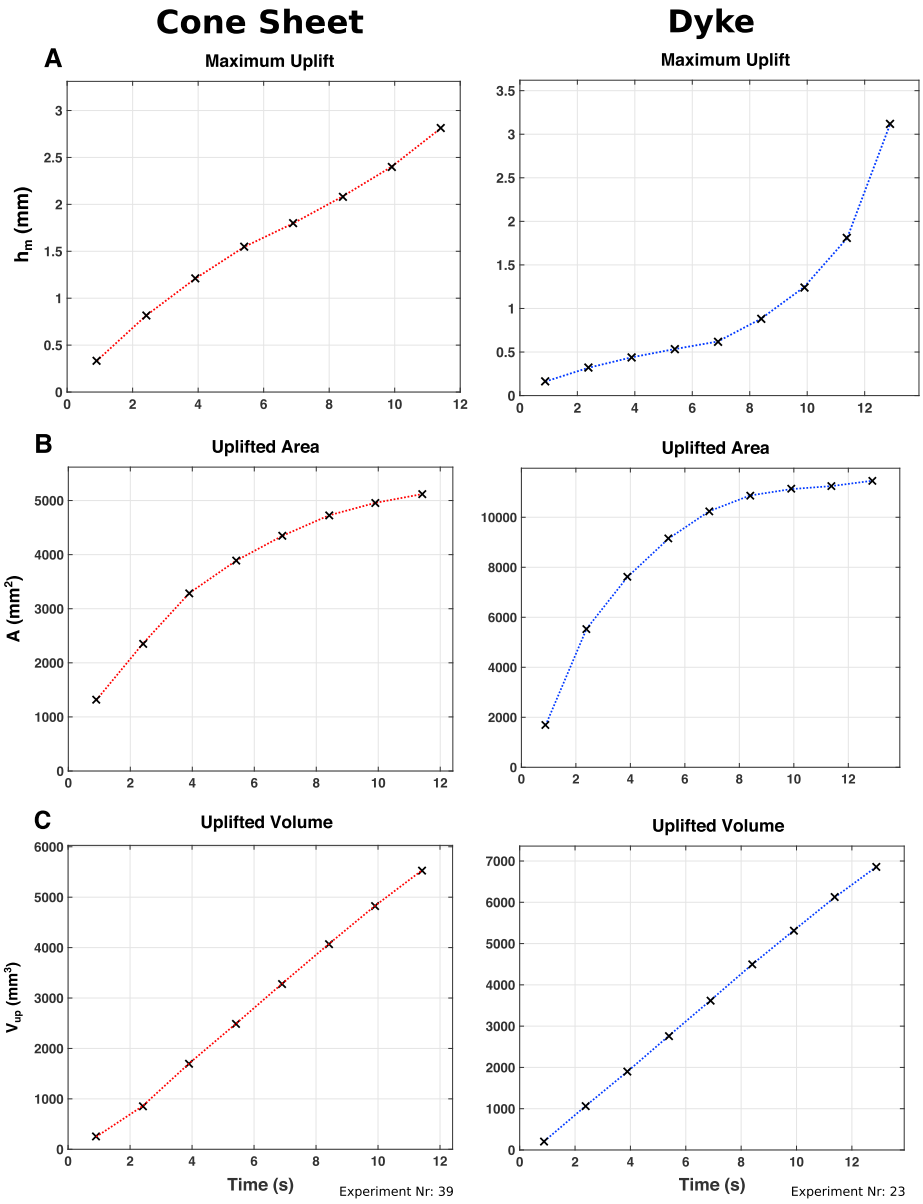

Figure 6. Raw data outputs from the ΔDEMs for (left) a representative cone sheet and (right) a dike experiment. As a function of time the graphs display the development of the (a) maximum uplift, (b) uplifted area, and (c) uplifted volume. The dike was produced using an inlet width of 0.5 cm, a D_i = 6 cm, and an injection velocity of ca 80 mL/min. The cone sheet was produced using an inlet width of 0.2 cm, a D_i = 2 cm, and an injection velocity of ~20 mL/min.

h_m also vary significantly from one experiment to another. Therefore, we also scale the evolution of h_m for each experiment by the final maximum uplift h_f, such that h_m/h_f may vary from 0 (no uplift) to 1 (final uplift).

The relative uplift h_m/h_f as a function of τ for all the experiments shows that dikes and cone sheets display two systematically distinct behaviors (Figure 7). The h_m/h_f for most of the cone sheets shows a relatively rapid initial increase, a subsequent gentle deceleration, followed by an almost linear increase of h_m/h_f from $\tau \sim 0.2$ until the eruption. Dike experiments instead show that h_m/h_f exhibits an initial moderate to low increase that suddenly accelerates from τ of about 0.5–0.8. The exception is one dike experiment that peaks immediately before eruption. However, unlike the other dike models, large open fractures developed at the surface of this experiment before the oil erupted.

Relevant scaling is also useful to analyze the temporal evolution of the uplifted area, *A*. According to the theoretical models of Mogi (1958) and Sun (1969), among others, the radius of an uplifted area that is associated

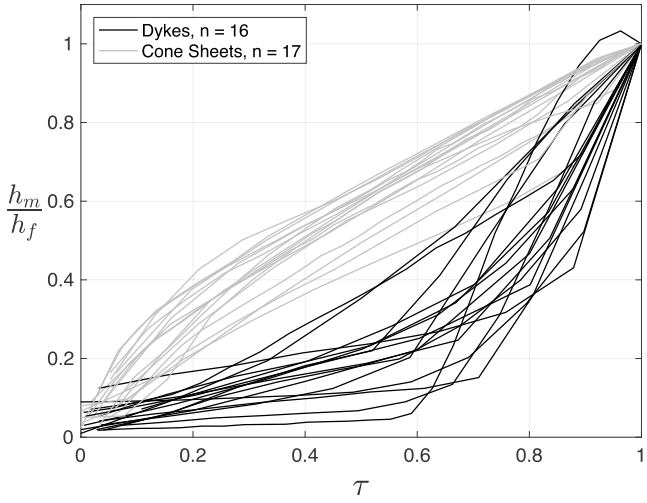

Figure 7. Plot of the normalized maximum uplifts versus dimensionless time for 18 of the cone sheet (gray) and 17 of the dike (black) experiments. The shortest experiments, for which less than five differential digital elevation models (ΔDEMs) are available, are not shown. Two end-member behavioral regimes can be distinguished. After an initial rapid increase that slows down, most of the maximum uplift above cone sheets develops gradually and quasi-linearly. In contrast, the maximum uplift above dikes exhibits a more pronounced two-phase evolution with an initial slow increase that suddenly accelerates from about the half, or more, of the experiment duration.

with the inflation of a deep magma source is proportional to the depth of the source. Therefore, we scaled A by D_i^2 (Figure 8). The evolution of A/D_i^2 for the dike and cone sheet experiments exhibits similar shapes (see also Figure 6). However, the obtained values of A/D_i^2 are usually larger for cone sheets than for dikes, illustrating that the scaled uplifted area is generally larger above cone sheets than above dikes.

A different approach is used to scale the uplifted volume. Since the oil is injected at a constant flow rate, the volume of injected oil through time V_{inj} can be calculated. Therefore, we defined the ratio $\Delta V/V_{inj} = (V_{up} - V_{inj})/V_{inj}$, which is the difference in uplifted volume versus injected volume scaled by the injected volume. This ratio quantifies to what extent that the deformation due to the volume of injected oil is accommodated by an uplift of the model surface. The $\Delta V/V_{inj} = 0$ implies that the flour only deforms by uplift of its surface as a result of the oil intrusion, whereas $\Delta V/V_{inj} = -1$ indicate no uplift, that is, that the oil intrusion is only accommodated by deformation of the flour at depth. Our results show that the obtained values of $\Delta V/V_{inj}$ are generally larger for the cone sheets (from ~0 to ~ −0.6, −0.3 on average) than for the dikes (from ~ −0.2 to ~ −1, −0.7 on average; Figure 9). This difference indicates that the intrusion of cone sheets dominantly induces surface uplift as a response to the oil intrusion, whereas dikes more likely induce internal deformation of the flour with moderate surface uplift relative to the quantity of injected oil. Nevertheless, several values of $\Delta V/V_{inj}$ overlap for dikes and cone sheets.

During oil intrusion in all the experiments, surface deformation progressively develops an asymmetry (Figures 4 and 10). When a dike forms, the uplifted area is initially symmetrical, and the uplift is of relatively low amplitude. Subsequently, an asymmetric uplift initiates from one side of the uplifted area, and most of the uplift focuses at a bulge that moves to the margin of the uplifted areas (Figure 10b). In the cone sheet experiments, the initial uplifted area is also symmetrical. However, in contrast with the dikes, asymmetry develops gradually (Figure 10c).

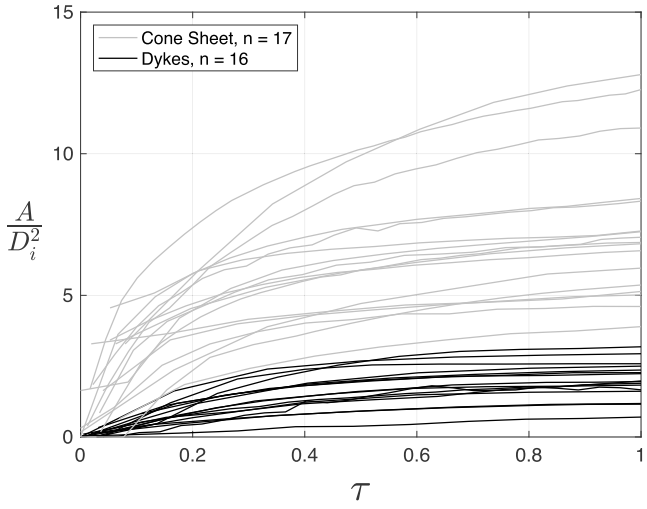

Figure 8. Plots of the uplifted area scaled by the square of the oil source depths versus normalized time for the cone sheet (gray) and dike (black) experiments (the shortest dike experiment lasting for less than five time steps is not shown). The cone sheets generally result in a larger scaled uplifted area than dikes.

To quantify the asymmetrical development of the surface deformation patterns associated with dikes and cone sheets, we defined the center of the uplifted area and calculated the distances between the center and each pixel of the uplifted area at each time step. This allows for plotting the global distribution of the uplift as a function of the distance to the center of the uplifted area for all time steps of the experiments (Figure 11). For both the dike and cone sheet experiments, the data exhibit very little dispersion at the first time steps, illustrating that the uplifted areas are symmetrical. For the next time steps the data show more dispersion, indicating that the uplifted areas become asymmetrical. For the ultimate time steps, the asymmetries are distinctive for dike and cone sheet experiments. The distribution of the data for the dike experiments shows a local development of most of the uplift, compared to a more distributed overall uplift characterizing the cone sheets.

At each time step of each experiment, we computed the averaged distribution of the uplift (Figure 11), representing the distribution for a virtual ideally symmetrical uplifted area. Then we calculated the standard deviation, σ, from the virtual symmetrical profile over the entire distribution for each time step. Small σ values indicate a low dispersion of the uplifts and a rather symmetrical uplifted area

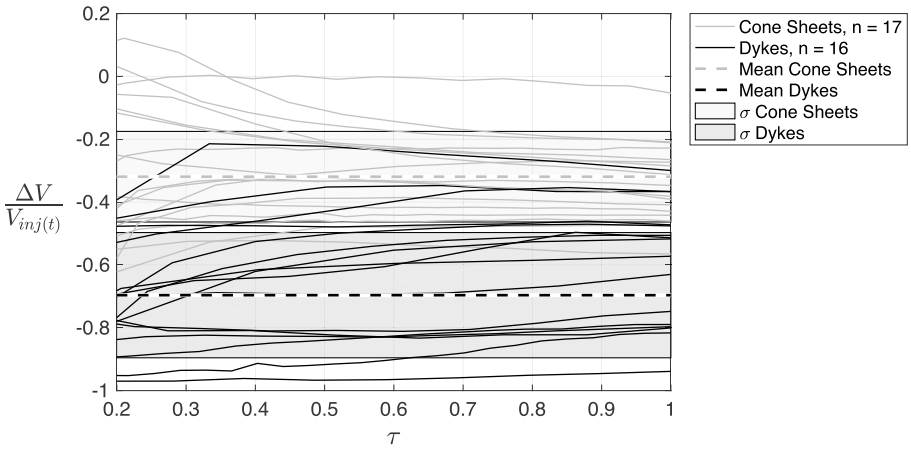

Figure 9. Ratio of uplifted volume minus the injected oil volume normalized by the injected volume versus the dimensionless time for cone sheet (gray) and dike (black) experiments. The shortest experiments are not shown. The dashed lines indicate the respective means and the shaded areas the respective standard deviation, σ. Some of the dikes induce very weak surface deformation relative to the volume of injected. In contrast, for some of the cone sheets, the uplifted volume roughly corresponds to the injected volume. Initial time steps are omitted because of amplified noise due to scaling.

(Figure 11, top row), whereas large σ values indicate high dispersion with a substantial asymmetry of the uplifted area (Figure 11, bottom row).

To compare the experiments, we scale the σ values at each time step by the value σ_f obtained for the final time step of each experiment. Figure 12 displays the temporal evolutions of σ/σ_f for most of the experiments.

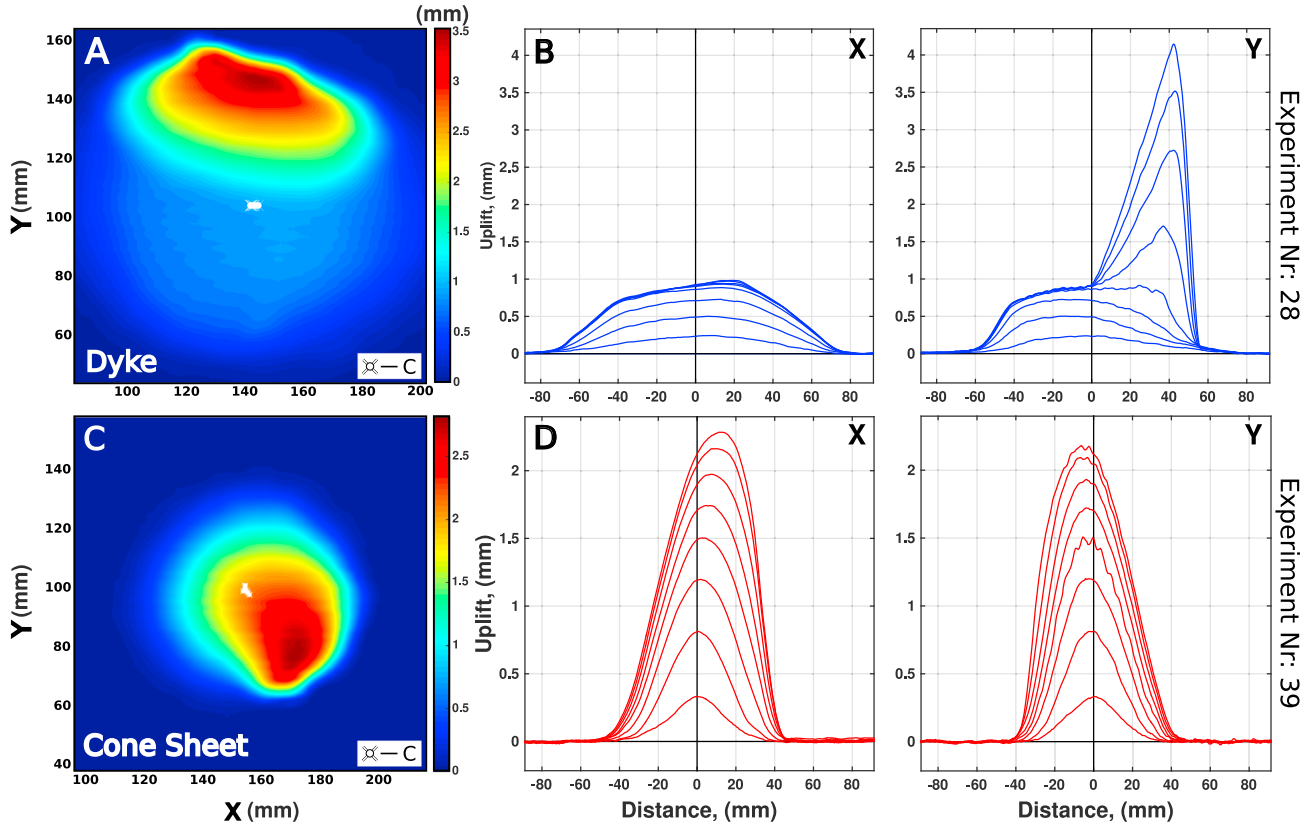

Figure 10. (a and c) Maps of the final surface elevations observed for a representative dike and a cone sheet experiment. The white crosses locate the mean centers (C) of the uplifted area at each time step during the experiments. (b and d) Successive profiles along the (left) *x* and (right) *y* reference directions and passing through the centers C at each time step for the corresponding experiments: dike (Figure 10b) and cone sheet (Figure 10d). Maps and profiles show a cropped area limited to the affected uplifted area. The dike was produced using an inlet width of 0.5 cm, a $D_i = 7$ cm, and an injection velocity of ~120 mL/min. The cone sheet was produced using an inlet width of 0.2 cm, a $D_i = 2$ cm, and an injection velocity of ~20 mL/min.

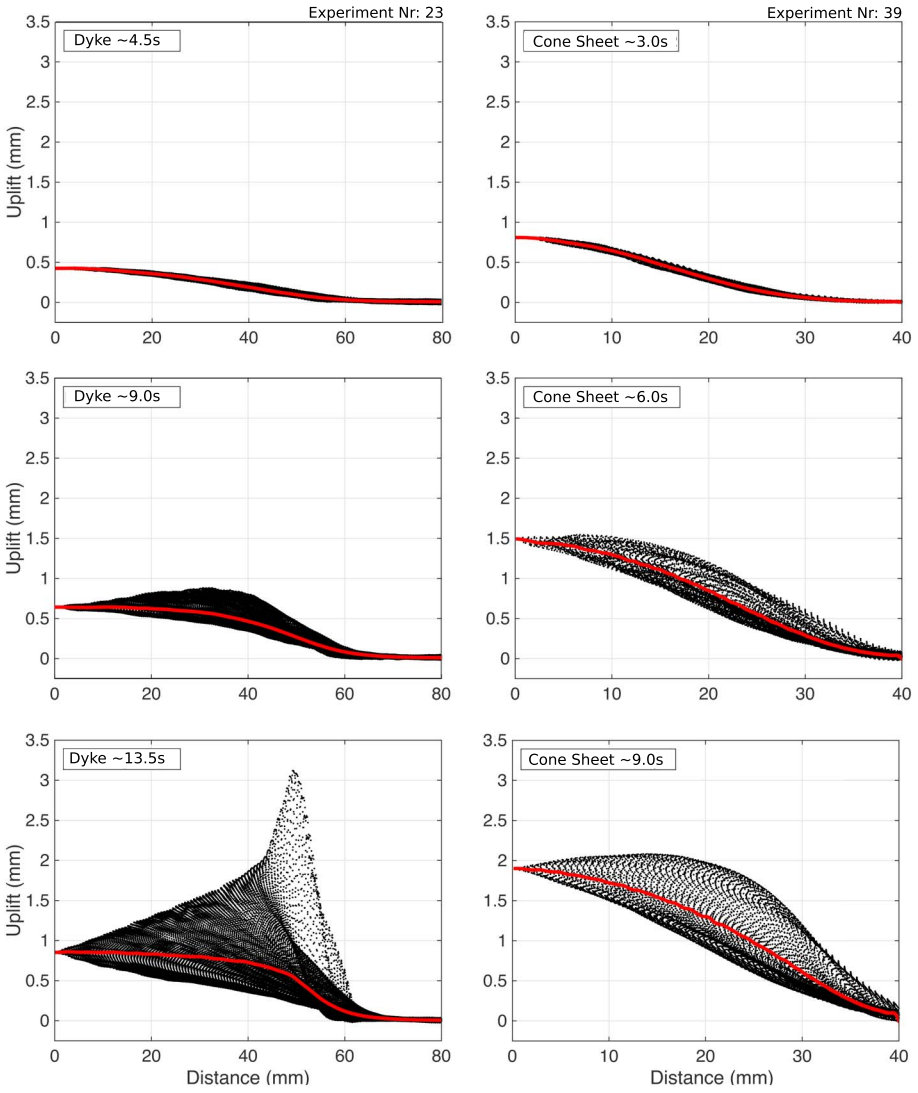

Figure 11. Plots of the observed uplift as a function of the distance to the center of the uplifted area for (left column) a dike and (right column) a cone sheet experiment, at early, intermediate, and late time steps. The red line corresponds to the mean distribution of the uplifts, representative of an ideal symmetrical dome, from which a residual standard deviation is calculated to quantify the degree of asymmetry at each time step for each experiment. The dike was produced using an inlet width of 0.5 cm, a D_i = 6 cm, and an injection velocity of ~80 mL/min. The cone sheet was produced using an inlet width of 0.2 cm, a D_i = 2 cm, and an injection velocity of ~20 mL/min.

Cone sheet and dike experiments again exhibit distinct behaviors. For most cone sheets, a nearly linear increase of σ/σ_f occurs from $\tau > 0.2$ (Figure 12). In all cases, the asymmetry of the uplifted area develops gradually from the early stages of the intrusions. In contrast, for most of the dikes σ/σ_f remains very low until τ reaches about 0.5 to 0.7, values from which σ/σ_f rapidly increases. For dikes, the uplifted area remains relatively symmetrical until at least half of the experiment duration, followed by the development of a significant asymmetry prior to the eruption.

4. Interpretation and Discussion

4.1. Interpretation

The distinct gradual or two-phase development of h_m/h_f (Figure 7) and σ/σ_f (Figure 12) for cone sheets and dikes, respectively, correlates with the final shapes of the underlying intrusions described by Galland et al. (2014). The surface deformation associated with cone sheets exhibits a gradual, almost

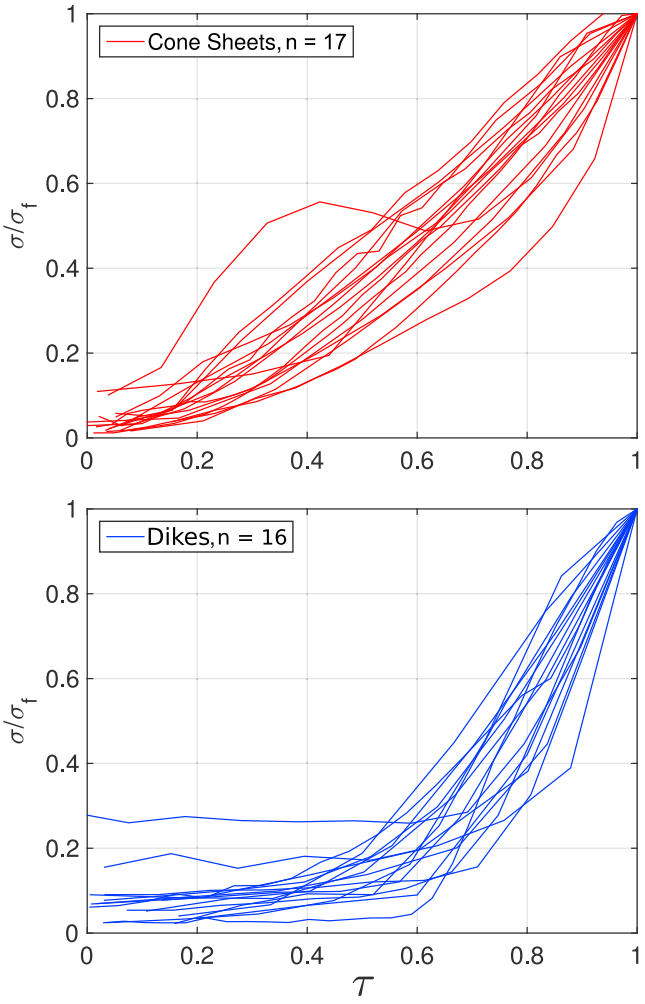

Figure 12. Standard deviation of the observed uplift normalized to the final standard deviation of the uplift versus dimensionless time, for (top) 17 cone sheet (red) and (bottom) 16 dike (blue) experiments. Only experiments with more than four time steps have been plotted. Two dominating trends emerge; cone sheets gradually develop while dikes display a two-stage evolution.

continuous evolution, whereas that of dikes is clearly two-phase, with a first symmetrical, low-amplitude uplift followed by a second phase of asymmetrical, rapid localized uplift. In addition, the excavated dikes often displayed either an inclined sheet or a hull-shaped termination just below the model surface, and above the underlying subvertical main dike (Galland et al., 2014). Such dike shapes are interpreted as resulting from two successive intrusion regimes, as illustrated by the emplacement of an initial, deep subvertical dike, the tip of which bifurcates or splits at a critical depth to form either the inclined sheet or hull-shaped intrusion. It is thus inferred that the two-stage evolution of the dike surface deformation may correlate with such a two-stage evolution. Such a hypothesis is in good agreement with the two-dimensional experiments of Mathieu et al. (2008) and Abdelmalak et al. (2012), who showed that the shallow splitting of a propagating dike tip induces both uplift acceleration and asymmetry. Similar behaviors have also been observed in fluid pipes (aka sand injectites; Mourgues et al., 2012) and conduits of fluids propagating from depth within the oceanic crust to the seafloor (Gay et al., 2012). Similar two-stage behavior associated with a shallow dike-to-sill transition has been inferred in the Afar rift (Magee et al., 2017; Pagli et al., 2012). Conversely, the gradual and sublinear evolution of surface deformation associated with cone sheet emplacement is likely the result of the continuous emplacement during a single regime of sheet intrusion growing gradually from the inlet.

The overall patterns of evolution of the uplifted area and volume are similar for both intrusion types (Figures 8 and 9). However, relative to the inlet depth, D_i, cone sheets generate larger uplifted areas than dikes. Similarly, the ratio $\Delta V/V_{inj}$ reaches much larger values for cone sheets than for dikes, indicating that the deformation due to cone sheet emplacement is mostly accommodated by uplift, in contrast to that due to most of the dikes. We thus infer from these results that cone sheets dominantly push their overburden upward, which is consistent with the current understanding of the formation of cone sheets (Burchardt et al., 2013; Klausen, 2004; Kuenen, 1937; Mathieu et al., 2008). This is in agreement with Galland et al. (2014), who showed that cone sheets preferentially form when the magmatic source exhibits a low depth-to-size ratio, that is, when it is shallow compared to its size. For dikes, our results suggest that the propagation is less influenced by the presence of a free surface, except in the second regime at shallow depth where the dike tip bifurcates or splits to form hull-shaped intrusions or inclined sheets. This is also consistent with the current understanding of the dike emplacement mechanics, in which deformation is thought to be dominantly accommodated by lateral pushing of the vertical walls, with a minor component of upward pushing (Abdelmalak et al., 2012; Kavanagh, Boutelier, & Cruden, 2015). This is also in agreement with Galland et al. (2014), who showed that dikes preferentially form when the magmatic source is deep compared to its size, and exhibits a high depth-to-size ratio (Figure 3). Deciphering between contrasting mechanisms could be possible through extracting horizontal surface displacements (e.g., Galland et al., 2016). However, the moiré projection monitoring system does not allow for quantification of the vertical and horizontal displacements separately.

Notably, the evolution of the overall asymmetry of uplift σ/σ_f (Figure 12) exhibits similar patterns to those shown by the evolution of h_m/h_f (Figure 7). This similarity suggests that the overall asymmetry of the surface uplift pattern is dominantly controlled by the behavior of the maximum uplift. It implies that tracking only the evolution of maximum uplifts is a good first-order indicator of the overall asymmetrical development of surface uplift patterns.

4.2. Discussion

The silica flour used in our experiments is a cohesive Coulomb material, which allows for both mode I and mode II fracturing, similar to natural rocks (Abdelmalak et al., 2016; Jaeger, Cook, & Zimmerman, 2009; Pollard, 1973). The cohesion, tensile strength, and friction coefficient of the silica flour can be measured easily and compared to those of natural rocks (Abdelmalak et al., 2016; Galland et al., 2006). Additionally, cohesive flours have the ability to stand nonnegligible elastic stresses along stable vertical walls (see Abdelmalak et al., 2016 and Figure S1 in the supporting information). In allowing for elasto-plastic deformation of the host, the experiments using flour show a major difference compared with laboratory models using elastic gelatine (e.g., Kavanagh, Menand, & Sparks, 2006; Rivalta & Dahm, 2006; Taisne & Jaupart, 2009; Takada, 1990, 1994; Tibaldi, Bonali, & Corazzato, 2014), most theoretical and numerical models (e.g., Galland & Scheibert, 2013; Maccaferri, Bonafede, & Rivalta, 2010; Pollard, 1987), and many geodetic models used to analyze surface deformation measured at active volcanoes, which assume purely elastic host (e.g., Mogi, 1958; Okada, 1985). However, the elastic properties of our silica flour are poorly constrained, which is also true for flours, in general. It is therefore challenging to decipher the elastic versus inelastic deformation due to intrusion in our models. In addition, compared to natural cases of intrusions, other features that our models do not account for include (1) host-rock heterogeneities, (2) topography (i.e., the model surface was flat), and (3) far field (i.e., tectonic) stresses.

Our results show that intrusion-induced deformation in our experimental cohesive Coulomb models is significantly affected by inelastic deformation, that is, shear failure. In contrast, established models of sheet intrusion propagation and geodetic models account for purely elastic deformation of the host rock. However, natural rocks are neither purely elastic nor purely Coulomb solids but are rather elasto-plastic materials (Gudmundsson, 2011; Jaeger et al., 2009), and one would expect that both deformation mechanisms are at work during magma propagation and emplacement. Even if the literature suggests (cf. Rubin, 1995) that inelastic deformation occurs during magma emplacement, a recurrent argument states that it is constrained to such a small volume near the dike tip that it can be assumed to have a negligible effect on propagation (Rubin, 1993). Nevertheless, recent field (Gudmundsson et al., 2008; Spacapan et al., 2017) and geophysical (Ágústsdóttir et al., 2016; White et al., 2011) observations of tip deformation demonstrate that shear failure significantly contributes to the propagation of sills and dikes, respectively. A relevant question is thus whether the local shear deformation at the intrusion tip significantly affects the overall deformation of the host rock.

In all the models of this study, the surface deformation accommodating magma emplacement occurred through surface uplifts regardless of the intrusion shape, including subvertical dikes. This is a major difference with elastic models of dike opening (e.g., Okada, 1985; Pollard & Holzhausen, 1979), which predict a local trough, that is, surface subsidence, above the dike tip. We interpret the different surface deformation patterns in terms of contrasting subsurface host deformation modes; in our models the silica flour is expected to fail through the formation of shear fractures induced by the flow of the viscous vegetable oil (Abdelmalak et al., 2012; Donnadieu & Merle, 1998; Mathieu et al., 2008). This mechanism, the so-called *viscous indenter*, implies that the magma creates its own space by pushing the host rock ahead of the intrusion tip, resulting in surface uplift. Natural examples supporting this mode of propagation involve intruding magma of probable andesitic composition, that is, magma with relatively high viscosities (Spacapan et al., 2017). In this specific example, the intrusions appear to have propagated by pushing the host rocks ahead and the dike tips exhibit blunt or rectangular shapes. This is in stark contrast with the sharp, narrow tips expected for tensile elastic fractures (Figure 13). The blunting of an intrusion tip likely occurs when the host rock exhibits an elasto-plastic rheology, as demonstrated by Vachon and Hieronymus (2016). These observations thus validate the geological relevance of a propagation mechanism where a dike pushes its host rock ahead causing it to fail in shear, such as the *viscous indenter* mechanism, and so the use of cohesive silica flour in our experiments.

Our dike experiments initially display smooth dome-shaped surface uplift. Similar surface deformation has been recorded at Piton de la Fournaise volcano, Réunion Island (e.g., Cayol & Cornet, 1998; Froger et al., 2004; Toutain et al., 1992) and Galapagos (e.g., Amelung et al., 2000; Bagnardi, Amelung, & Poland, 2013). Mogi (1958) or inflating sill (e.g., Horizontal Okada) models are commonly used to fit such data. Our experimental results thus provide an alternative mechanism of surface uplift associated with the emplacement of a vertical dike through a Coulomb brittle crust.

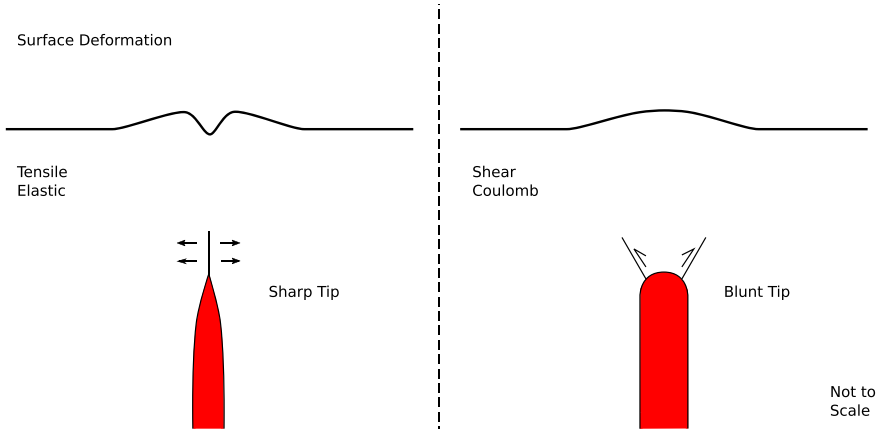

Figure 13. Profiles of conceptual surface deformation predicted by (left) a tensile elastic fracture compared to the surface deformation above (right) a subvertical sheet intrusion propagating due to shear failure in a Coulomb material.

The surface deformation associated with dike emplacement in rift zones often display two bulges and a trough parallel to an underlying dike (Figure 13). Such deformation has been monitored at Krafla, Iceland (e.g., Hollingsworth et al., 2012); Afar (e.g., Grandin et al., 2010; Wright et al., 2012); and at the Harrat Lunayyir basaltic field, Saudi Arabia (Pallister et al., 2010). Because such surface deformation is compatible with the elastic deformation expected from the Okada source model, the Okada (1985) model is commonly used to model surface deformation patterns associated with dike emplacement in rifts. However, the Okada source model's far-field stress boundary conditions do not account for regional tectonic extension, which is clearly at work in active rift zones. This discrepancy between boundary conditions in active rifts and in the Okada model questions whether the observed subsidence during rifting episodes is triggered by the emplacement of the dike or by regional extensional tectonics.

Finally, our models and their proposed interpretations are mostly relevant for volcanic systems where (1) the magma viscosity is relatively high, that is, andesitic to rhyolitic compositions, and/or (2) the host rock is composed of relatively weak, poorly consolidated rocks, such as tephra or tuff, which are common in differentiated volcanic systems, and/or tuffites or poorly consolidated sedimentary rocks, which are common host rocks to volcanic plumbing systems emplaced in sedimentary basins (e.g., Spacapan et al., 2017). Thus, our model and modeled uplifts may not apply to all geological settings.

5. Conclusion

This paper describes the systematic analysis of surface deformation patterns induced by the emplacement of dikes and cone sheets into a cohesive, Coulomb brittle crust. The data come from 43 experiments of the experimental series presented by Galland et al. (2014), who performed a systematic parameter study identifying the conditions at which dikes and cone sheets preferentially form, in simulating the intrusion of relatively viscous magma into a relatively weak host at shallow depth. The main conclusions from our study are the following:

1. Both the emplacement of dikes and cone sheets induce surface uplift.
2. Uplift associated with cone sheet emplacement is higher than that associated with dike emplacement. Cone sheets, which generally initiate at shallower depth, dominantly push their host upward while the deeper dikes emplace through lateral opening of their host.
3. The evolution of surface deformation patterns associated with dike and cone sheet emplacement exhibits systematic, distinct signatures.
4. Cone sheet emplacement induces a gradual, quasi-linear uplift; the initial uplift shows a symmetrical bell-shaped pattern, which gradually develops an asymmetry until eruption.
5. Conversely, dike emplacement induces two-stage surface uplift; the initial uplift is low, and the uplift pattern remains symmetrical; at shallower depth (about halfway through the experiment duration), uplift suddenly increases and grows rapidly, developing a strongly asymmetrical uplift pattern.

6. All the experimental dikes induced uplift, and no subsidence of the surface above the dikes was observed, in contrast with the predictions of common elastic models.
7. The Coulomb behavior of the Earth's brittle crust may significantly affect the surface deformation patterns of shallow intrusions.
8. The temporal evolution of the maximum uplift can be used as a proxy for the overall development of surface deformation.

Our laboratory results suggest that it may be necessary to account for the Coulomb brittle behavior of the Earth's crust to satisfactorily interpret geodetic measurements associated with shallow magma intrusions.

Acknowledgments
Guldstrand's position is funded by the DIPS project (grant 240467) from the Norwegian Research Council. Burchardt acknowledges financial support from V. R. Troll, Uppsala University, the Swedish Research Council for a research visit to PGP. Hallot acknowledges his welcome to PGP for several weeks, thanks to a half-year sabbatical, teaching-free CRCT from Université de Rennes 1. The data analysis was performed in the framework of an exchange visiting grant (grant 4251) through the MeMoVolc Networking Programme, funded by the European Science Foundation. The data are available here: https://doi.org/10.5281/zenodo.898692. We acknowledge the constructive reviews of Claudia Corrazato, Mike Poland, an anonymous reviewer, and the Associate Editor of JGR: Solid Earth, which greatly improved the manuscript. Guldstrand would like to acknowledge Fanny Bjugger for assistance in laboratory work and in discussions. Guldstrand would also like to acknowledge the Volcano Plumbing Systems group at PGP, University of Oslo, for fruitful, enthusiastic, and stimulating discussions.

References

Abdelmalak, M., Bulois, C., Mourgues, R., Galland, O., Legland, J.-B., & Gruber, C. (2016). Description of new dry granular materials of variable cohesion and friction coefficient: Implications for laboratory modeling of the brittle crust. *Tectonophysics*, *684*, 39–51. https://doi.org/10.1016/j.tecto.2016.03.003

Abdelmalak, M., Mourgues, R., Galland, O., & Bureau, D. (2012). Fracture mode analysis and related surface deformation during dyke intrusion: Results from 2D experimental modelling. *Earth and Planetary Science Letters*, *359*, 93–105.

Ágústsdóttir, T., Woods, J., Greenfield, T., Green, R. G., White, R. S., Winder, T., … Soosalu, H. (2016). Strike-slip faulting during the 2014 Bárðarbunga-Holuhraun dike intrusion, central Iceland. *Geophysical Research Letters*, *43*, 1495–1503. https://doi.org/10.1002/2015GL067423

Amelung, F., Jónsson, S., Zebker, H., & Segall, P. (2000). Widespread uplift and 'trapdoor' faulting on Galapagos volcanoes observed with radar interferometry. *Nature*, *407*(6807), 993–996.

Bagnardi, M., Amelung, F., & Poland, M. P. (2013). A new model for the growth of basaltic shields based on deformation of Fernandina volcano, Galápagos Islands. *Earth and Planetary Science Letters*, *377*, 358–366.

Bréque, C., Dupre, J.-C., & Bremand, F. (2004). Calibration of a system of projection moiré for relief measuring: Biomechanical applications. *Optics and Lasers in Engineering*, *41*(2), 241–260.

Burchardt, S., Troll, V. R., Mathieu, L., Emeleus, H. C., & Donaldson, C. H. (2013). Ardnamurchan 3D cone-sheet architecture explained by a single elongate magma chamber. *Scientific Reports*, *3*, 2891.

Cayol, V., & Cornet, F. H. (1998). Three-dimensional modeling of the 1983–1984 eruption at Piton de la Fournaise Volcano, Réunion Island. *Journal of Geophysical Research*, *103*(B8), 18,025–18,037.

Chadwick, W. W., Jónsson, S., Geist, D. J., Poland, M., Johnson, D. J., Batt, S., … Ruiz, A. (2011). The May 2005 eruption of Fernandina volcano, Galápagos: The first circumferential dike intrusion observed by GPS and InSAR. *Bulletin of Volcanology*, *73*(6), 679–697.

Donnadieu, F., & Merle, O. (1998). Experiments on the indentation process during cryptodome intrusions: New insights into Mount St. Helens deformation. *Geology*, *26*(1), 79–82.

Dzurisin, D. (2006). *Volcano Deformation: New Geodetic Monitoring Techniques*. Chichester, UK: Springer Science & Business Media.

Froger, J. L., Fukushima, Y., Briole, P., Staudacher, T., Souriot, T., & Villeneuve, N. (2004). The deformation field of the August 2003 eruption at Piton de la Fournaise, Reunion Island, mapped by ASAR interferometry. *Geophysical Research Letters*, *31*, L14601. https://doi.org/10.1029/2004GL020479

Galland, O. (2012). Experimental modelling of ground deformation associated with shallow magma intrusions. *Earth and Planetary Science Letters*, *317*, 145–156.

Galland, O., & Scheibert, J. (2013). Analytical model of surface uplift above axisymmetric flat-lying magma intrusions: Implications for sill emplacement and geodesy. *Journal of Volcanology and Geothermal Research*, *253*, 114–130.

Galland, O., Bertelsen, H. S., Guldstrand, F., Girod, L., Johannessen, R. F., Bjugger, F., … Mair, K. (2016). Application of open-source photogrammetric software MicMac for monitoring surface deformation in laboratory models. *Journal of Geophysical Research: Solid Earth*, *121*, 2852–2872. https://doi.org/10.1002/2015JB012564

Galland, O., Burchardt, S., Hallot, E., Mourgues, R., & Bulois, C. (2014). Dynamics of dikes versus cone sheets in volcanic systems. *Journal of Geophysical Research: Solid Earth*, *119*, 6178–6192. https://doi.org/10.1002/2014JB011059

Galland, O., Cobbold, P. R., Hallot, E., de Bremond d'Ars, J., & Delavaud, G. (2006). Use of vegetable oil and silica powder for scale modelling of magmatic intrusion in a deforming brittle crust. *Earth and Planetary Science Letters*, *243*(3), 786–804.

Galland, O., Planke, S., Neumann, E.-R., & Malthe-Sørenssen, A. (2009). Experimental modelling of shallow magma emplacement: Application to saucer-shaped intrusions. *Earth and Planetary Science Letters*, *277*(3), 373–383.

Gay, A., Mourgues, R., Berndt, C., Bureau, D., Planke, S., Laurent, D., … Loggia, D. (2012). Anatomy of a fluid pipe in the Norway Basin: Initiation, propagation and 3D shape. *Marine Geology*, *332*, 75–88.

Grandin, R., Socquet, A., Jacques, E., Mazzoni, N., de Chabalier, J. B., & King, G. (2010). Sequence of rifting in Afar, Manda-Hararo rift, Ethiopia, 2005–2009: Time-space evolution and interactions between dikes from interferometric synthetic aperture radar and static stress change modeling. *Journal of Geophysical Research*, *115*, B10413. https://doi.org/10.1029/2009JB000815

Gudmundsson, A. (2011). *Rock Fractures in Geological Processes*. Cambridge, UK: Cambridge University Press.

Gudmundsson, A., Friese, N., Galindo, I., & Philipp, S. L. (2008). Dike-induced reverse faulting in a graben. *Geology*, *36*(2), 123–126.

Haug, Ø. T., Galland, O., Souloumiac, P., Souche, A., Guldstrand, F., & Schmiedel, T. (2017). Inelastic damage as a mechanical precursor for the emplacement of saucer-shaped intrusions. *Geology*. https://doi.org/10.1130/G39361.1

Hollingsworth, J., Leprince, S., Ayoub, F., & Avouac, J. P. (2012). Deformation during the 1975–1984 Krafla rifting crisis, NE Iceland, measured from historical optical imagery. *Journal of Geophysical Research*, *117*, B11407. https://doi.org/10.1029/2012JB009140

Jaeger, J. C., Cook, N. G., & Zimmerman, R. (2009). *Fundamentals of Rock Mechanics*. Malden, MA: John Wiley & Sons.

Kavanagh, J., Boutelier, D., & Cruden, A. (2015). The mechanics of sill inception, propagation and growth: Experimental evidence for rapid reduction in magmatic overpressure. *Earth and Planetary Science Letters*, *421*, 117–128.

Kavanagh, J. L., Menand, T., & Sparks, R. S. J. (2006). An experimental investigation of sill formation and propagation in layered elastic media. *Earth and Planetary Science Letters*, *245*(3), 799–813.

Klausen, M. (2004). Geometry and mode of emplacement of the Thverartindur cone sheet swarm, SE Iceland. *Journal of Volcanology and Geothermal Research*, *138*(3), 185–204.

Kuenen, P. H. (1937). Intrusion of cone-sheets. *Geological Magazine*, *74*, 177–183.
Maccaferri, F., Bonafede, M., & Rivalta, E. (2010). A numerical model of dyke propagation in layered elastic media. *Geophysical Journal International*, *180*(3), 1107–1123.
Magee, C., Bastow, I. D., de Vries, B. V. W., Jackson, C. A.-L., Hetherington, R., Hagos, M., & Hoggett, M. (2017). Structure and dynamics of surface uplift induced by incremental sill emplacement. *Geology*, *45*(5), 431–434.
Mathieu, L., de Vries, B. V. W., Holohan, E. P., & Troll, V. R. (2008). Dykes, cups, saucers and sills: Analogue experiments on magma intrusion into brittle rocks. *Earth and Planetary Science Letters*, *271*(1), 1–13.
Mogi, K. (1958). Relations between the eruptions of various volcanoes and the deformations of the ground surfaces around them. *Bulletin of the Earthquake Research Institute*, *36*, 99–134.
Mourgues, R., Bureau, D., Bodet, L., Gay, A., & Gressier, J. (2012). Formation of conical fractures in sedimentary basins: Experiments involving pore fluids and implications for sandstone intrusion mechanisms. *Earth and Planetary Science Letters*, *313*, 67–78.
Okada, Y. (1985). Surface deformation due to shear and tensile faults in a half-space. *Bulletin of the Seismological Society of America*, *75*(4), 1135–1154.
Pagli, C., Wright, T. J., Ebinger, C. J., Yun, S.-H., Cann, J. R., Barnie, T., & Ayele, A. (2012). Shallow axial magma chamber at the slow-spreading Erta Ale Ridge. *Nature Geoscience*, *5*(4), 284.
Pallister, J. S., McCausland, W. A., Jónsson, S., Lu, Z., Zahran, H. M., El Hadidy, S., … White, R. A. (2010). Broad accommodation of rift-related extension recorded by dyke intrusion in Saudi Arabia. *Nature Geoscience*, *3*(10), 705–712.
Pollard, D. D. (1973). Derivation and evaluation of a mechanical model for sheet intrusions. *Tectonophysics*, *19*(3), 233–269.
Pollard, D. D. (1987). Elementary fracture mechanics applied to the structural interpretation of dykes, In H. C. Halls & W. F. Fahrig (Eds.), *Mafic Dyke Swarms, Geological Association of Canada Special Paper* (Vol. 34, pp. 5–24).
Pollard, D. D., & Holzhausen, G. (1979). On the mechanical interaction between a fluid-filled fracture and the Earth's surface. *Tectonophysics*, *53*(1–2), 27–57.
Rivalta, E., & Dahm, T. (2006). Acceleration of buoyancy-driven fractures and magmatic dikes beneath the free surface. *Geophysical Journal International*, *166*(3), 1424–1439.
Rubin, A. M. (1993). Tensile fracture of rock at high confining pressure: Implications for dike propagation. *Journal of Geophysical Research*, *98*(B9), 15,919–15,935.
Rubin, A. M. (1995). Propagation of magma-filled cracks. *Annual Review of Earth and Planetary Sciences*, *23*, 287–336.
Scheibert, J., Galland, O., & Hafver, A. (2017). Inelastic deformation during sill and laccolith emplacement: Insights from an analytic elasto-plastic model. *Journal of Geophysical Research: Solid Earth*, *122*, 923–945. https://doi.org/10.1002/2016JB013754
Sigmundsson, F., Hooper, A., Hreinsdóttir, S., Vogfjörd, K. S., Ófeigsson, B. G., Heimisson, E. R., … Gudmundsson, G. B. (2015). Segmented lateral dyke growth in a rifting event at Bar [eth] arbunga volcanic system, Iceland. *Nature*, *517*(7533), 191–195.
Spacapan, J. B., Galland, O., Leanza, H. A., & Planke, S. (2017). Igneous sill and finger emplacement mechanism in shale-dominated formations: A field study at Cuesta del Chihuido, Neuquén Basin, Argentina. *Journal of the Geological Society*, *174*(3), 422–433. https://doi.org/10.1144/jgs2016-056
Sun, R. J. (1969). Theoretical size of hydraulically induced horizontal fractures and corresponding surface uplift in an idealized medium. *Journal of Geophysical Research*, *74*(25), 5995–6011.
Taisne, B., & Jaupart, C. (2009). Dike propagation through layered rocks. *Journal of Geophysical Research*, *114*, B09203. https://doi.org/10.1029/2008JB006228
Takada, A. (1990). Experimental study on propagation of liquid-filled crack in gelatin: Shape and velocity in hydrostatic stress condition. *Journal of Geophysical Research*, *95*(B6), 8471–8481.
Takada, A. (1994). Development of a subvolcanic structure by the interaction of liquid-filled cracks. *Journal of Volcanology and Geothermal Research*, *61*(3), 207–224.
Tibaldi, A., Bonali, F., & Corazzato, C. (2014). The diverging volcanic rift system. *Tectonophysics*, *611*, 94–113.
Toutain, J. P., Bachelery, P., Blum, P. A., Cheminee, J. L., Delorme, H., Fontaine, L., … Taochy, P. (1992). Real time monitoring of vertical ground deformations during eruptions at Piton de la Fournaise. *Geophysical Research Letters*, *19*(6), 553–556.
Trippanera, D., Acocella, V., & Ruch, J. (2014). Dike-induced contraction along oceanic and continental divergent plate boundaries. *Geophysical Research Letters*, *41*, 7098–7104. https://doi.org/10.1002/2014GL061570
Vachon, R., & Hieronymus, C. F. (2016). Effect of host-rock rheology on dyke shape, thickness, and magma overpressure. *Geophysical Journal International*, ggw448, 1414–1429.
White, R. S., Drew, J., Martens, H. R., Key, J., Soosalu, H., & Jakobsdóttir, S. S. (2011). Dynamics of dyke intrusion in the mid-crust of Iceland. *Earth and Planetary Science Letters*, *304*(3), 300–312.
Wright, T. J., Sigmundsson, F., Pagli, C., Belachew, M., Hamling, I. J., Brandsdóttir, B., … Ebinger, C. (2012). Geophysical constraints on the dynamics of spreading centres from rifting episodes on land. *Nature Geoscience*, *5*(4), 242–250.